Imageless Shape Detection Using a Millimeter-Wave Dynamic Antenna Array and Noise Illumination

Daniel Chen, *Graduate Student Member, IEEE*, Stavros Vakalis, *Graduate Student Member, IEEE*, and Jeffrey A. Nanzer, *Senior Member, IEEE*

***Abstract*—We present a dynamic millimeter-wave antenna array with rotational dynamics to detect shapes in a scene without image formation. The rotationally dynamic two-element receiving array is able to capture responses in the spatial Fourier (spatial frequency) domain corresponding to sharp edges in the spatial domain. By implementing a dynamic rotation of 180°, a ring-shaped filter is obtained in the spatial frequency domain. Sharp edges in a scene manifest broad spatial spectral responses that are localized at specific spatial frequency angles and extend radially outward. The ring filter is orthogonal to these strong responses, and thus captures them as a function of spatial frequency angle. Shapes with multiple sharp edges produce responses at angles orthogonal to the edge direction, thereby supporting the ability to classify objects based only on the strength and angular location of the spatial frequency responses. Accurate representation of the spatial Fourier domain requires the scattered fields to be spatially and temporally incoherent, thus we transmit noise signals from multiple separate noise transmitters, thereby illuminating the scene with incoherent radiation. The dynamic antenna array thus obtains a high signal-to-noise ratio on the received signals, allowing the use of traditional, low-gain millimeter-wave hardware. We evaluate the concept experimentally with a 38-GHz, two-element dynamic antenna array. We demonstrate the detection of spatial frequency signals via rotational dynamics for several reflecting targets of different shape. The results demonstrate good agreement with simulations and further support the feasibility of detecting shapes in a scene without image formation.**

***Index Terms*—Dynamic antennas, millimeter-wave imaging, millimeter-wave radar, noise radar, interferometry, sparse arrays, spatial frequency**

I. Introduction

The detection of objects in a scene is an important aspect in a broad range of millimeter-wave imaging applications, including contraband detection in security sensing [1], [2], environmental sensing for autonomous vehicles [3], [4], human-computer interaction [5], [6], and airborne remote sensing [7], [8], among many others. Millimeter-wave technology is beneficial for such applications since the wavelengths of the radiation are sufficiently short to provide high resolution, while also being sufficiently long that they propagate through obscurants such as clothing, garments, fog, and smoke [9]. As millimeter-wave sensing becomes more ubiquitous in society, the ability to detect and classify objects without compromising personal privacy is attracting increasing interest. Traditional imaging approaches form full images of scenes, after which signal processing algorithms are applied to the formed images for shape detection and classification. This approach not only may include privacy concerns, but is also inefficient, since full images are formed when the objects of interest may only occupy a small fraction within recovered images.

Approaches that allow for shape detection and recognition, without relying on full image reconstruction, are thus of interest. However, detecting and classifying the spatial shape of objects without forming spatial information inherently necessitates the use of sensing or information acquisition in an alternative domain or dimension. A promising approach is to sense the scene in the Fourier transform domain, or the spatial frequency domain. Recently, we explored the theoretical potential for detecting Fourier-domain artifacts of objects with sharp edges [10]. In the spatial frequency domain, sharp edges manifest broad-spatial-spectral responses that are localized to spatial frequency domain angles orthogonal to the spatial direction of the edges. We found that the responses for common man-made structures such as buildings in microwave images of the ground produce responses that could be captured by sampling only a small segment of spatial frequency domain information, far less than that are needed for full image reconstruction. In [11] we derived a ring-shaped spatial frequency filter that could be obtained using a two-element antenna array with rotational dynamics, and demonstrated the ability to classify ground scenes between those containing man-made structures and those without. Recently, we presented the first experimental demonstration of a millimeter-wave system designed to detect the Fourier domain artifacts of objects [12]. Aside from these works, to our knowledge, no other works have investigated imageless object detection for sensing applications.

In this work, we present a 38 GHz dynamic antenna array and demonstrate the detection of unique Fourier domain signatures of a wide range of different reflecting objects. Appropriate sampling of spatial frequency information requires the signals scattered from the scene to be spatially and temporally incoherent. To support this, we combine our dynamic antenna array with the recently developed active incoherent millimeter-wave (AIM) imaging concept, where noise transmission is

Manuscript received 2021.

This material is based upon work supported by the National Science Foundation under grants 1708820 and 1751655. This paper is an expanded version from the 2021 International Microwave Symposium, Atlanta, GA, USA. *(Corresponding author: Jeffrey A. Nanzer)*

The authors are with the Department of Electrical and Computer Engineering, Michigan State University, East Lansing, MI 48824 USA (email: chendan7@msu.edu; vakaliss@msu.edu; nanzer@msu.edu).

used to illuminate the scene with spatio-temporally incoherent radiation while also achieving received signal gains that are detectable using low-gain receiver hardware [13]–[15].

Three noise transmitters are used along with two receiving antennas on a rotating structure (see Fig. 1). The dynamic rotation of the array generates a narrow, ring-shaped filter in the spatial frequency domain that captures the broad spatial-spectral responses resulting from sharp edges of objects. Unlike other interferometric imaging approaches, the rotational dynamic antenna array requires only two receiving antennas. By linearizing the ring-filtered responses as function of the dynamic antenna array's rotated angle, a polar diagram of the measured responses thus provides inference to determine the edge direction and potential shapes of the measured target. We expand on our prior work by developing the dynamic antenna array theory more thoroughly, presenting a detailed description of the 38 GHz system, and demonstrating the detection of a larger set of unique objects. We first describe the active interferometric imaging technique, and then present the proposed rotational dynamic antenna array with experimental measurements to demonstrate successful identification of unique spatial frequency signatures of six metal-shaped targets. Differences in the one-dimensional spatial frequency filter responses demonstrate the ability to identify aspects of the two-dimensional shape of the objects. Our imageless shape detection approach has the following important aspects:

- The technique uses only two compact receive antenna elements and array dynamics to detect two-dimensional shapes, significantly reducing the hardware impact compared to other millimeter-wave imaging techniques that rely on electrically large apertures with large numbers of antenna elements.
- The detection approach is computationally efficient since no image formation is required. Object detection operates on one-dimensional signals 1-D Fourier transforms, which requires orders of magnitude less computational time than 2-D spatial image reconstruction, either through beamscanning [16] or by solving an inverse problem [17].
- The technique is privacy-preserving: the approach does not generate full images and furthermore does not capture sufficient information to form a full image. Thus, privacy concerns that are present in other high-resolution millimeter-wave imaging techniques for security and contraband imaging are absent in our approach.

II. Interferometric Imaging

Of the various millimeter-wave imaging techniques, Fourier domain interferometric imaging, which samples information in the spatial frequency domain and uses inverse Fourier processing to reconstruct the scene intensity, has seen growing interest due to its capability to generate high-resolution imagery while requiring only a small fraction of the aperture area typically required by imaging approaches such as the mechanically- and/or electronically-steered antennas or focal plane arrays [18]–[20]. Sampling the Fourier domain spatial frequency information of a given scene is achieved by cross-correlating the received signals between the multiple antenna

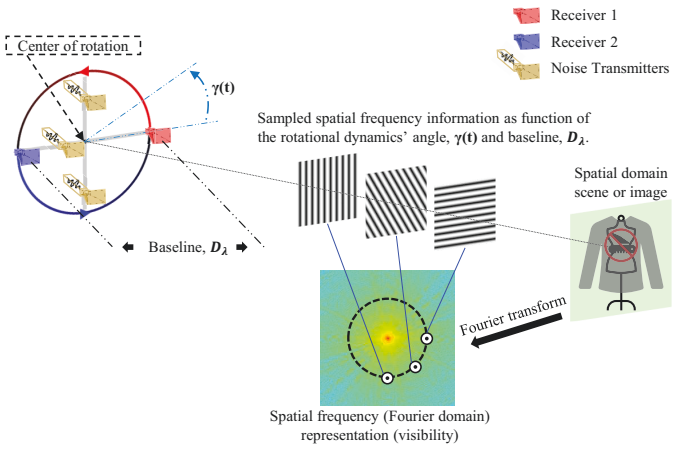

Fig. 1. Overview on the system concept of the implemented millimeter-wave rotational dynamic antenna array. The two receiving antennas (red and blue) co-rotate in counterclockwise direction with respect to their centroid to dynamically synthesize the proposed ring filter in the spatial frequency domain. The sampled spatial frequency information is dependent on the rotationally dynamic angle $\gamma(t)$ and the baseline separation D_λ between the two receiving antennas which is illustrated by the three far field grating lobe patterns in the middle of the diagram that corresponds to a specific spatial frequency sample point as illustrated on the visibility.

pairs in a sparse antenna array. An array of N receiving elements has $\frac{N}{2}(N-1)$ unique antenna pairs, thus the number of spatial frequency samples can be very large, even when the number of physical elements in the array is small. This results in dense sampling functions yielding high-resolution image reconstruction using very sparse antenna arrays [21]–[24].

Interferometric imaging systems collect Fourier domain information known as the scene *visibility* $V(u,v)$, where u and v are the two-dimensional (2D) variables in the spatial frequency plane. The visibility is the 2D Fourier transform of the scene intensity $I(\alpha,\beta)$, where $\alpha = \sin\theta\cos\phi$ and $\beta = \sin\theta\sin\phi$ are the associated direction cosines, and is given by

$$V(u,v) = \iint_{-\infty}^{+\infty} I(\alpha,\beta) e^{j2\pi(u\alpha+v\beta)} d\alpha d\beta. \tag{1}$$

Interferometric imaging systems capture a subset of the available visibility, defined by the sampling function $S(u,v)$, which is determined by the locations of the elements in the antenna array. The sampled visibility is the product between the scene visibility and the spatial frequency sampling function, and is obtained by cross-correlating the signals received at a given pair of antennas in the array. The reconstructed scene intensity can then be recovered via inverse Fourier transform of the sampled visibility:

$$I_r(\alpha,\beta) = \iint_{-\infty}^{+\infty} V(u,v) S(u,v) e^{-j2\pi(u\alpha+v\beta)} du dv. \tag{2}$$

While (1) and (2) are in continuous form, the sampling function is however discrete in general since the antennas are located at discrete positions in space. For a 2D spatial frequency plane, specific u and v locations being sampled are

related to the spatial x and y locations of receiving antennas through $u = D_x/\lambda$ rad^{-1} and $v = D_y/\lambda$ rad^{-1}, where D_x and D_y are the antenna baselines in the spatial x and y dimensions of a particular antenna pair where the wavelength of the received radiation is $\lambda = c/f$. The complete collection of all discretely acquired 2D spatial frequency information is called the sampling function that can be expressed as follows:

$$S(u,v) = \sum_{n=1}^{N}\sum_{m=1}^{M}\delta(u-u_n)\delta(v-v_m), \tag{3}$$

where the quantity NM represents the maximum number of spatial frequency information that the interferometric imaging array can collect and $\delta(\cdot)$ is the delta function.

The signals from the scene may be generated intrinsically via thermal radiation [25], or via active illumination of the scene [13], however, as indicated by the Van Cittert-Zernike theorem [26] they must be incoherent in both space and time to support accurate sampling of the visibility. Passive interferometric imaging systems capture thermal radiation, which is inherently incoherent across space and time [27]–[30], however the radiated thermal power is exceedingly small at millimeter-wave frequencies, necessitating the use of very high sensitivity receivers. In contrast, active interferometric systems transmit spatio-temporally uncorrelated signals to illuminate the scene of interest in order to obtain sufficient received power thus typical low-cost receivers can be used [13]–[15].

As the visibility is the Fourier transform of the scene intensity, objects with discrete spatial responses (edges) will result in spatial frequency signals that are broad spectrum, but located along angles orthogonal to the edge, as shown in Fig. 2 where a sharp edge (a) and its visibility (b) are plotted. Since the visibility response extends in the (u,v) plane from $(0,0)$ outward, any narrow filter in the orthogonal direction will be able to detect the response. Objects with multiple edges will produces responses at various angles which is demonstrated by the pair shown in Fig. 2(c) and (d), indicating that a ring-shaped filter can be used to capture the responses from sharp edges as a function of angle. Note that this approach essentially captures sidelobe structures from scenes with strong discrete spatial signals; however the placement of the ring filter ensures that strong responses near spatial dc do not impact the processing. Notably, while such filter can detect the Fourier domain artifacts resulting from the spatial domain information, this subset of spatial frequency information is insufficient to reconstruct the full image, thus providing a mechanism for object detection without image formation.

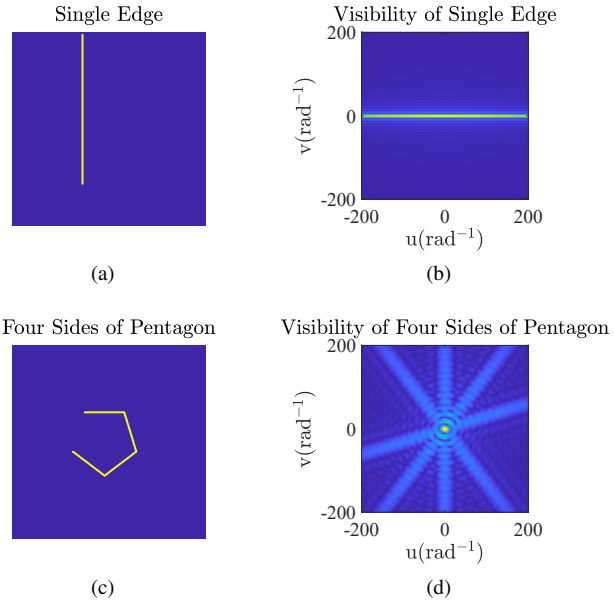

Fig. 2. Theoretical visibilities of simple shapes demonstrating the broad spatial spectral responses of sharp edges. (a) Single sharp edge. (b) Visibility of the single sharp edge where the single broad spectrum spatial frequency signal that is orthogonal to the edge direction is shown. (c) Four sides (edges) of a pentagon. (d) Visibility of the pentagon with four sides demonstrating that multiple discrete spatial responses (edges) produces corresponding spatial frequency responses. Note that the missing fifth side (edge) is intended to demonstrate the orthogonal relationship to the broad spectrum spatial frequency signal in the associated visibility.

III. Fourier Domain Sensing Using a Dynamic Antenna Array

While interferometric imaging arrays utilize significantly less antenna elements than traditional phased arrays, using antenna dynamics enables the formation of a denser sampling function with as few as two receiving antenna elements. This concept was used in passive interferometric imaging applications for early radio astronomy measurements to generate dense sampling functions via the rotation of the Earth [22]. The rotation dynamics of the Earth are, however, slow and unalterable as a design parameter, and nonetheless irrelevant outside of astronomical observations. In contrast, motivated by recent developments on the use of fast platform dynamics to reduce grating lobes in distributed phased arrays [31], [32], we recently proposed the use of relatively fast rotational dynamics on a two-element interferometric array to synthesize a ring filter in the spatial frequency domain [11]. This approach also results in the use of less millimeter-wave hardware by a large factor: typical interferometric imaging arrays use at least 24 elements, often more, thus the use of only two elements significantly reduces hardware expenses. In this work, we realize the dynamic array approach with a 38 GHz millimeter-wave dynamic antenna array combined with three noise transmitters.

Fig. 1 shows the system concept of the rotational dynamic antenna array with two receiving antennas indicated in red and blue (separated by baseline D_λ) that co-rotate counter-clockwise with regard to their centroid. Three transmitting antennas are also implemented on the dynamic antenna array to leverage the AIM technique to properly illuminate the scene of interest with incoherent radiation. As the two-element dynamic antenna array rotates, the sampled spatial frequency information location in the uv-space also changes as function of time dependent angle $\gamma(t)$ and the designed baseline separation, D_λ. This aspect of changing spatial frequency sampling location is demonstrated by the three far field grating lobe patterns from left to right in the middle of Fig. 1 that correspond to the rotational dynamics at different instances. Each grating lobe pattern corresponds to a specific spatial frequency sample point as illustrated on the visibility example

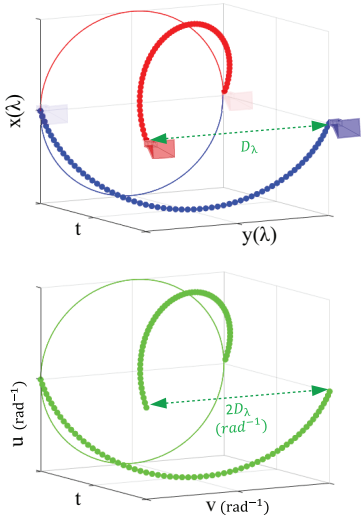

Fig. 3. (a) Rotational dynamics of a two-element array (red/blue) where the receiving antennas are separated by D_λ for one complete rotation in counterclockwise direction. (b) Corresponding synthesized spatial frequency sampling function corresponding to the same instances of the array's rotational dynamics where every half rotation (180° rotation) yields a complete ring filter, hence, a full rotation of the dynamic antenna array synthesizes two complete ring filters. Note the correlation between the dynamic antenna array and the synthesized ring filter's counterclockwise rotational dynamics.

of a simulated scene.

The concept to synthesize a ring filter in the spatial frequency domain is shown in Fig. 3. A two-element dynamic interferometric array is rotated counterclockwise (top) to synthesize the corresponding ring filter in the spatial frequency domain (bottom). Due to symmetry, a counterclockwise rotation of only 180° is required to form a full 360° ring filter in the spatial frequency domain. Note that the radius of the ring filter is determined by the baseline separation D_λ and that the direction of rotational dynamics is a design choice.

As the spatial frequency sampling function is determined by the pair-wise baseline vectors of the antennas and the rotational dynamics, the ring filter generated by the proposed two-element rotational dynamic antenna array can be expressed in terms of the designed antenna baseline D_{ring} and the set of K rotational angles, $\gamma(k)$ for $k = 0, 1, ..., K-1$, by

$$u_k = D_{ring} \sin \gamma(k), \tag{4}$$

and

$$v_k = D_{ring} \cos \gamma(k), \tag{5}$$

where the discrete rotational angles $\gamma(k)$ can be expressed using the initial angle of the dynamic array γ_0, the rotational rate γ_r, and the integration time τ for each spatial frequency sample which takes the form of

$$\gamma(k) = \gamma_0 + \gamma_r k\tau. \tag{6}$$

Thus, by modifying (3) with the spatial frequency sampling points defined by the rotational dynamics from (4)-(6), the

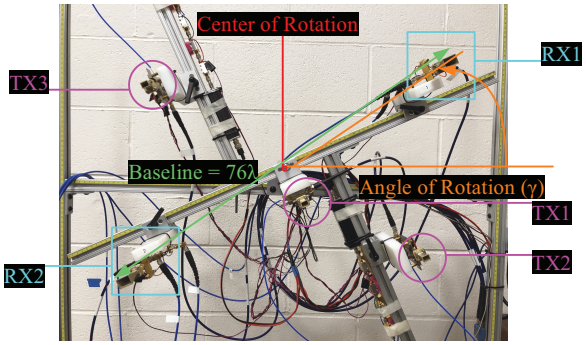

Fig. 4. Photograph of the implemented dynamic antenna array. The placement of the transmitting (TX) and receiving (RX) antennas are essentially as shown in Fig. 1. The system is implemented with a 76λ baseline separation (green) between the two receiving antennas (cyan squares). The receivers and three noise transmitting antennas (magenta circles) are all placed on a rotating arm that supports 180° rotation, sufficient for sampling the full visibility. The particular setup is capable to generate a ring filter of 76λ (rad^{-1}) radius in 180° rotation as demonstrated in Fig. 3. The center of rotation is in red and that the rotating angle with respect to the horizontal plane is in orange.

ring filtering sampling function of the two-element rotational dynamic antenna array can be given by

$$S_{ring}(u, v) = \sum_{k=0}^{K-1} \delta(u - u_k)\, \delta(v - v_k). \tag{7}$$

Let δ_k represent the sampled visibility at spatial angle k. The collection of all ring filtered visibility V_{ring} sampled over K sequentially rotated angles can then be considered as a series of sequential spatial frequency samples around the ring that is associated with the dynamic array's rotation such that

$$V_{ring,K} = \{\delta_0, \delta_1, \delta_2, ...\delta_{K-1}\}. \tag{8}$$

By computing the magnitude for each independent entry in the sampled visibility series described by (8), a linearized relationship between the spatial rotation and the sampled spatial frequency information can be obtained for edge shape identification via

$$l_{ring}(k) = \{|V_{ring,K}|\}. \tag{9}$$

IV. Experimental System Design

The experimental setup of the rotational dynamic antenna array is shown in Fig. 4 where two receiving antennas (RX1 and RX2 in cyan), separated by a designed baseline of 76λ (green), and the three noise transmitting antennas (TX1–TX3 in magenta) are all integrated on the same rotating structure to ensure co-polarization with the receiving antennas. The designed receiver separation of 76λ is based on the concept demonstrated in [11] where baseline must ensure that the discrete spectral signals related to sharp edges exhibit sufficient signal strength compared to the surrounding visibility. The center of rotation (red) is at the centroid between the two receiving antennas and angle of rotation γ (orange) is referenced to the horizontal plane which also shows a counterclockwise rotation dynamics of the overall setup. The system is designed to operate at 38 GHz where the designed baseline of 76λ ($\approx$ 60 cm) between the two receiving antennas

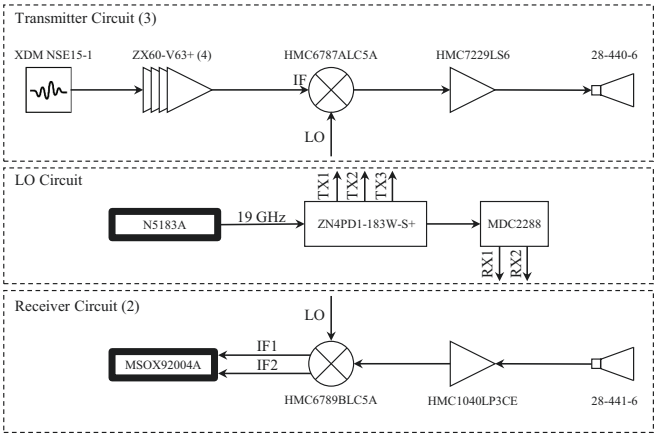

Fig. 5. Radio frequency schematic of the major subsystems of the rotational dynamic antenna array. The role of the noise sources is to enable spatio-temporally incoherent illumination of the scene. The upconverters and downconverters enable the system implementation to be experimentally feasible at millimeter-wave bands (i.e., 38 GHz) with a compact design. Top: Circuit for one transmitter node. Middle: Circuit for the 19 GHz local oscillator. Bottom: Circuit for one receiver node. Number in parenthesis indicates the quantity. IF: Intermediate frequency. LO: Local Oscillator. TX: Transmitter. RX: Receiver.

can be compactly obtained. The proposed ring filter is thus achieved over a 180° rotation as demonstrated in Fig. 3.

The radio frequency (RF) schematics of the major subsystems of the rotational dynamic antenna array system are shown in Fig. 5. To satisfy the spatio-temporally incoherent illumination of the scene, each of the three transmitting nodes comprises a 10–1600 MHz noise source (RF-GADGETS XDM NSE15-1) where the noise signal is fed through four cascaded wideband amplifiers (Mini-Circuits ZX60-V63+) before being fed to the intermediate frequency (IF) port of an upconverter, the HMC6787ALC5A from Analog Devices. This upconverter is desirable for its integrated frequency doubling feature on the signal provided to its local oscillator (LO) port; hence, a 19 GHz LO is designed to mix with the described baseband noise to generate a 38 GHz carrier at the upconverter's output port. The upconverted mixed signal at 38 GHz is subsequently fed to a Analog Devices HMC7229LS6 to achieve noise power level of approximately -10 dBm which is then fed to a standard gain 10 dBi horn antenna made by L3Harris Narda-ATM (28-440-6). Each of the two receiving nodes comprises a standard gain 15 dBi horn antenna made by L3Harris Narda-ATM (28-441-6) that is connected to a 20 dB gain low-noise amplifier made by Analog Devices (HMC1040LP3CE). The amplified received signal is subsequently fed to a downconverter which is the Analog Devices HMC6789BLC5A that outputs an in-phase and quadrature (I/Q) signals. The selection of the specific upconverters and downconverters enable the system setup to be experimentally feasible at the millimeter-wave bands where a compact implementation is possible.

The five required LO signals, designed at 19 GHz for the three upconverters and two downconverters were generated using an Agilent N5183A signal generator that was first fed to a four-way splitter (Mini-Circuits ZN4PD1-183W-S+) where the first three split signals were fed to each of the LO port of the upconverters and the fourth output is further split through a two-way splitter (MIDISCO MDC2288). The two-way splitted outputs were then fed to the LO ports of the downconverters. The two pairs of I/Q baseband signals signals from each of the two downconverters were captured by a Keysight MSO-X92004A Infiniium High-Performance Oscilloscope and processed offline using MATLAB.

V. Experimental Results

All experimental measurements were conducted in a 7.6 m semi-enclosed arch range where the background walls were microwave absorbers. A standard digital angle gauge with 1° accuracy was fixed on the rotating portion of the experimental setup to track the rotation angle. A total of 180 measurements were taken per target in 1° increments that covers the top half of the uv-plane. Fabrication of the six measured targets were done by mounting reflective copper foil tape on foam boards that are effectively transparent at 38 GHz and were placed 1.83 m from the dynamic antenna array's broad side direction for measurement. Unless otherwise stated, individual targets were constructed using copper foil tape with a dimension of 5.1 cm $\times$ 61.0 cm. The back supporting square foam board had a side length of 61.0 cm. The sharp contrast between the copper foil tape and the transparent board enables the creation of shapes with identifiable spatial frequency signatures that can be used to validate the spare Fourier domain sampling approach using the described rotational dynamic antenna array concept.

A horizontal stripe (Fig. 6(a)) and a Chi-shape forming a 45° acute angle (Fig. 6(f)) were fabricated where their corresponding broad spectrum visibility responses in the Fourier domain at angles orthogonal to the physical direction of the shape edges (the mounted copper foil tapes) are shown in Fig. 6(b) and (g), respectively. In Fig. 6(c) and (h), the simulated ring-filtered visibilities using the implemented 76λ dynamic antenna array are shown where each is the product of the dynamically synthesized ring filter multiplied by the visibility of the corresponding target. The linearized ring filtered responses as described by (9) for the upper-half uv-plane from 0° to 180° are shown in Fig. 6(d) and (i) indicating the anticipated responses of the measurements. Shown in Fig. 6(e) are the measured linearized responses of the horizontal stripe (blue) along with a control scene as background with no reflective material (red) to demonstrate that the measured target had significant higher magnitude of reflected noise illumination than the referenced background. In Fig. 6(j), the measured linearized responses for the Chi-shape with 45° acute angle is shown. Both measured responses are evidently close to the simulated responses.

Common target movements can include translation or rotation. For the proposed dynamically synthesized ring filter, the translation of a target within the system's FOV does not manifest an angular shift in the Fourier domain for the visibility signatures that are being sparsely sampled. In contrast, the spatial rotation of target represents an angular shift of the orthogonal Fourier domain signatures. Therefore, a vertical stripe (Fig. 6(k)) was measured not only as an

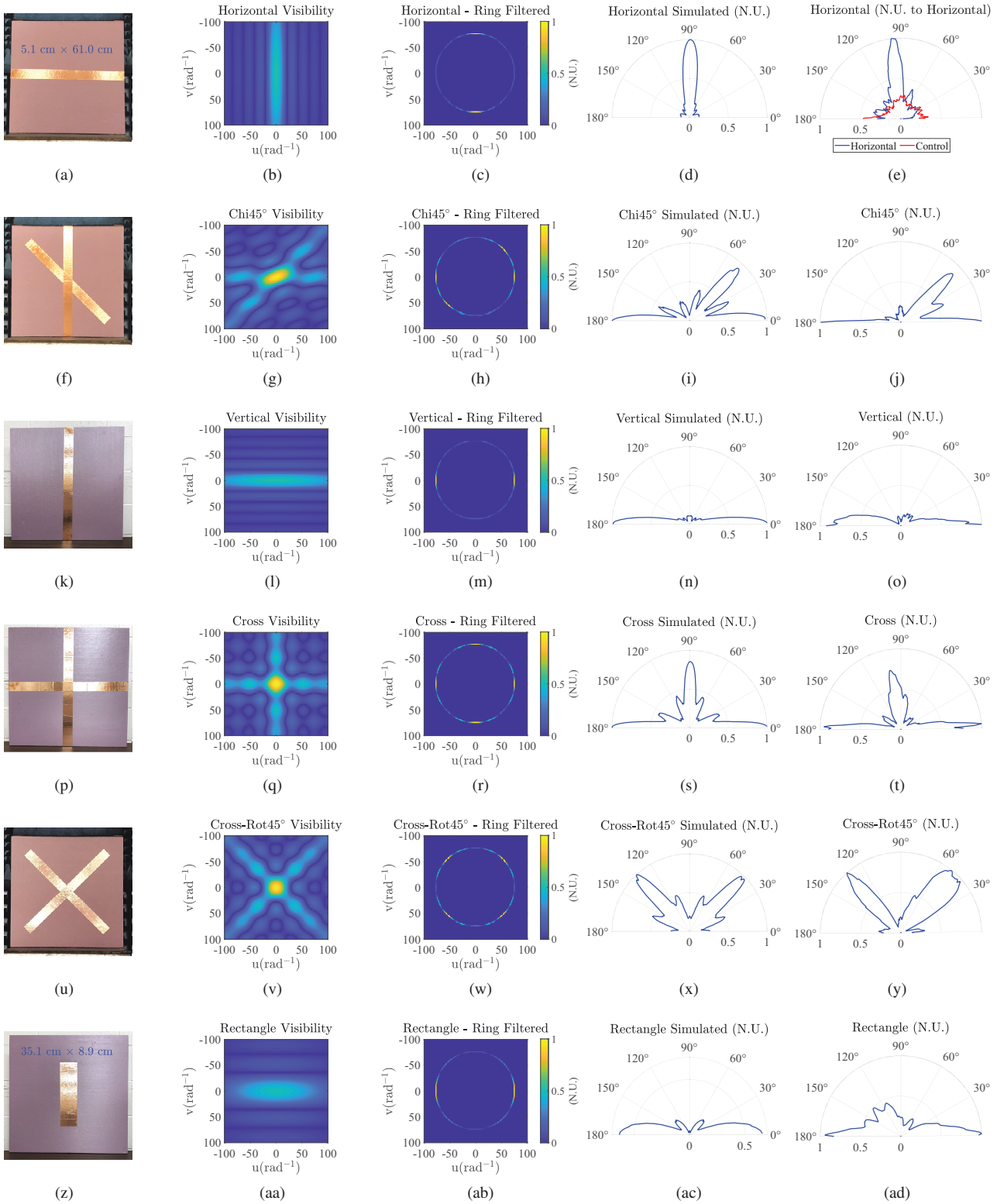

Fig. 6. Comparison of theoretical and experimental responses for various shapes measured with the 38 GHz system. Photographs of the fabricated targets are shown in the first column: (a) Horizontal stripe, (f) Chi-shape with 45° acute angle, (k) Vertical stripe, (p) Cross, (u) Cross rotated by 45°, and (z) Rectangle. The dimensions of all stripes in (a,f,k,p,u) are 5.1 cm × 61.0 cm; the dimensions of the stripe in (z) are 8.9 cm × 35.1 cm. The second column shows the visibility from (1) corresponding to the targets. The third column shows the normalized simulated ring-filtered visibilities of the six targets using a 76λ ring filter. The fourth column shows the simulated linearized ring-filtered responses as a function of rotation angle for the upper-half of the uv-plane. The fifth column shows the measurement results where (e) also contains a background measurement as a control test (shown in red) demonstrating that the measured target had significant higher magnitude of reflected noise illumination than the referenced background. All measurements (fifth column) closely resemble that of the simulated results (fourth column), validating the presented rotational dynamic antenna array concept to identify the shape of targets without image formation. N.U.: Normalized Units.

additional simple sharp-edged target but also as the horizontal stripe (Fig. 6(a)) that is spatially rotated by 90°. The associated visibility and the ring filtered visibility are shown in Fig. 6(l) and (m), respectively. The simulated linearized ring filtered responses as a function of the spatially rotated angle γ of the array is shown in Fig. 6(n) where the strong Fourier signatures captured at 76λ were also rotated by 90°. Similarly, the measurement result is shown in Fig. 6(o) with resemblance to the simulation and the expected 90° rotated Fourier domain signatures that are correlated to the considered spatial rotation of the horizontal stripe.

A measurement of a cross shape target was also made as a reference measurement to validate the rotated target scenario shown in Fig. 6(p) where the corresponding simulated visibility and ring filtered visibility are shown in Fig. 6(q) and (r), respectively. Fig. 6(s) is the simulated linearized response. Shown in Fig. 6(t) is the measurement result of the cross target showing close resemblance to the simulated results. With the cross target as a reference measurement, another cross target which is rotated spatially by 45° was also measured as shown in Fig. 6(u) with the simulated visibility and ring filtered visibility in Fig. 6(v) and (w). A simulated linearized response of the rotated cross target is shown in Fig. 6(x) where the Fourier signatures are shifted by 45° as expected. The measurement result is shown in Fig. 6(y) where close resemblance to the simulated results is again observed.

To gain further insight to the sharp-edge induced Fourier signatures, a comparison between targets with equal area but different physical dimension were also measured. The vertical stripe (Fig. 6(a)) was selected as the reference target which has a physical dimension of 61.0 cm by 5.1 cm. A comparison target that takes the form of a rectangle with physical dimension of 35.1 cm by 8.9 cm is shown in Fig. 6(z) with the corresponding simulated visibility and ring filtered visibility in Fig. 6(aa) and (ab). Linearized simulation results and measurement results are shown in Fig. 6(ac) and (ad), respectively.

The cross target can also be considered as the superposition of the horizontal and vertical stripes, in particular since the transmitted signals are incoherent, thus the superposition of the responses from separate targets should not result in constructive or destructive interference. In Fig. 7(a) the simulated result of the cross target from Fig. 6(s) (blue) is compared to the simulated result of superposing the ring-filtered responses between the horizontal and vertical stripes (red) from Fig. 6(d) and Fig. 6(n). While the responses from the cross and the superposed stripes are not exactly identical, the major Fourier signatures from the cross targets at angle 90° and 0° (180°) closely resemble that from the horizontal and vertical stripe, respectively. Similarly in Fig. 7(b), the measurement result of the cross target (blue) and the superposed result between the horizontal and vertical stripes (red) show close resemblance to each other while validating the simulated result. This result partly validates the incoherence of the transmitted signals, as the superposition of separate targets does not result in coherent interference.

In Fig. 7(c), the simulated linearized result of the vertical stripe is shown in blue and that of the rectangle with the same

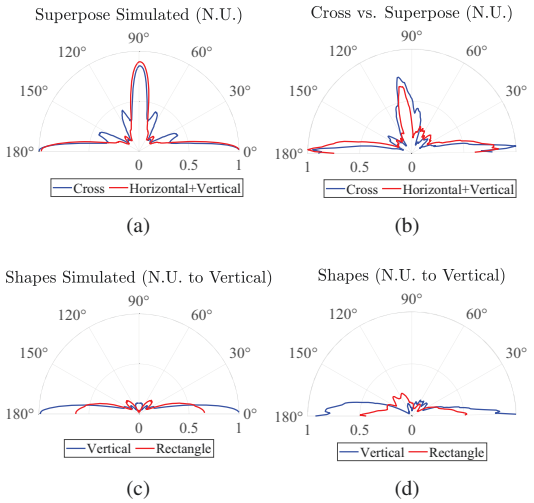

Fig. 7. (a) Comparison of the simulated results between the cross target in blue and superposing the horizontal and vertical stripes in red. (b) Comparison of the measured results between cross target in blue and superposing the horizontal and vertical stripes in red showing close resemblance to the simulations. (c) Comparison of the simulated results between the vertical stripe in blue and the rectangle in red where all responses are normalized to the vertical stripe to demonstrate that the sharp edge associated Fourier domain signatures changes as the dimension of the physical edge changes when using specific ring filter. (d) Comparison of the measured results between the vertical stripe in blue and the rectangle in red where similar reduction (as in (c)) of the measured signature's magnitude is observed.

physical area is shown in red with the responses normalized to the vertical stripe. It is noted that the major Fourier signatures at angles 0° (180°) of the rectangle exhibit lower magnitude compare to the reference vertical target at the same angles when considering a measurement using the 76λ ring filter. This is expected as the simulated visibility of the rectangle suggest narrower responses in the u-direction and broader responses in the v-direction, which when the same 76λ measuring ring filter is applied, different magnitudes of sharp-edge related Fourier responses are detected. The measurement results are shown in Fig. 7(d) with the vertical measurement in blue and the rectangle measurement in red. Similar decrease in magnitude of responses from vertical stripe to rectangle at angles 0° (180°) is observed.

VI. Conclusion

In this work, we presented a rotational dynamic antenna array concept that synthesize a ring-shaped filter in the spatial frequency domain. An experimental setup was implemented using commercially available RF components and common mounting and structural materials. Furthermore, experimental demonstration of unique signatures of multiple sharp-edged objects under different scenarios (rotating, superposing, shapes with equal area but different dimension) shows that objects can be identified using a dynamically rotated antenna array without full image reconstruction. The results provide a framework for imageless classification of objects using rotational dynamic antenna array sensing, where reduced information acquisition is sufficient to identify the shapes of objects while also using significantly less hardware. The concept may prove beneficial

for applications such as privacy-preserving security screening for air travel and large events.

REFERENCES

[1] S. Stanko, D. Notel, A. Wahlen, J. Huck, F. Kloppel, R. Sommer, M. Hagelen, and H. Essen, "Active and passive mm-wave imaging for concealed weapon detection and surveillance," in *2008 33rd International Conference on Infrared, Millimeter and Terahertz Waves*, 2008, pp. 1–2.

[2] C. Zheng, X. Yao, H. Anyong, and J. Miao, "Initial results of a passive millimeter- wave imager used for concealed weapon detection bhu-2d-u," *Prog. Electromagn. Res. C*, vol. 43, pp. 151–163, 01 2013.

[3] J. Hasch, E. Topak, R. Schnabel, T. Zwick, R. Weigel, and C. Waldschmidt, "Millimeter-wave technology for automotive radar sensors in the 77 ghz frequency band," *IEEE Trans. Microw. Theory Techn.*, vol. 60, no. 3, pp. 845–860, Mar. 2012.

[4] R. H. Rasshofer and K. Gresser, "Automotive radar and lidar systems for next generation driver assistance functions," *Adv. Radio Sci.*, vol. 3, no. B. 4, pp. 205–209, May 2005.

[5] J. Lien, N. Gillian, M. E. Karagozler, P. Amihood, C. Schwesig, E. Olson, H. Raja, and I. Poupyrev, "Soli: Ubiquitous gesture sensing with millimeter wave radar," *ACM Trans. Graph.*, vol. 35, no. 4, pp. 1–19, Jul. 2016.

[6] S. Hazra and A. Santra, "Robust gesture recognition using millimetric-wave radar system," *IEEE Sens. Lett.*, vol. 2, no. 4, pp. 1–4, Dec. 2018.

[7] J. P. P. Gomes, J. F. B. Brancalion, and D. Fernandes, "Automatic target recognition in synthetic aperture radar image using multiresolution analysis and classifiers combination," in *2008 IEEE Radar Conference*, 2008, pp. 1–5.

[8] U. Srinivas, V. Monga, and R. G. Raj, "Sar automatic target recognition using discriminative graphical models," *IEEE Trans. Aerosp. Electron. Syst.*, vol. 50, no. 1, pp. 591–606, Jan. 2014.

[9] J. A. Nanzer, *Microwave and Millimeter-Wave Remote Sensing for Security Applications*. Artech House, 2012.

[10] D. Chen, S. Vakalis, V. Holmes, and J. A. Nanzer, "Spatial frequency filter design for interferometric image classification without image reconstruction," in *2020 IEEE USNC-CNC-URSI North American Radio Science Meeting (Joint with AP-S Symposium)*, 2020, pp. 23–24.

[11] D. Chen, S. Vakalis, and J. A. Nanzer, "Dynamic antenna array design for scene classification through fourier-domain filtering," *IEEE Trans. Antennas Propag.*, vol. 69, no. 9, pp. 5953–5962, Sep. 2021.

[12] D. Chen, S. Vakalis, and J. A. Nanzer, "A millimeter-wave dynamic antenna array for classifying objects via sparse fourier domain sampling," in *2021 IEEE/MTT-S International Microwave Symposium (IMS)*, 2021.

[13] S. Vakalis and J. A. Nanzer, "Microwave imaging using noise signals," *IEEE Trans. Microw. Theory Techn.*, vol. 66, no. 12, pp. 5842–5851, Dec. 2018.

[14] S. Vakalis, L. Gong, and J. A. Nanzer, "Imaging with wifi," *IEEE Access*, vol. 7, pp. 28 616–28 624, 2019.

[15] S. Vakalis, L. Gong, Y. He, J. Papapolymerou, and J. A. Nanzer, "Experimental demonstration and calibration of a 16-element active incoherent millimeter-wave imaging array," *IEEE Trans. Microw. Theory Techn.*, vol. 68, no. 9, pp. 3804–3813, Sep. 2020.

[21] K. Schulz, D. Brunner, and M. Boldt, "Comparison of covamcoh and ilu image products for interferometric very high resolution sar image pairs," in *2011 IEEE International Geoscience and Remote Sensing Symposium*, 2011, pp. 313–315.

[16] B. Ku, P. Schmalenberg, O. Inac, O. D. Gurbuz, J. S. Lee, K. Shiozaki, and G. M. Rebeiz, "A 77–81-ghz 16-element phased-array receiver with $\pm 50^\circ$ beam scanning for advanced automotive radars," *IEEE Trans. Microw. Theory Tech.*, vol. 62, no. 11, pp. 2823–2832, Nov. 2014.

[17] A. Ribes and F. Schmitt, "Linear inverse problems in imaging," *IEEE Signal Process. Mag.*, vol. 25, no. 4, pp. 84–99, Jul. 2008.

[18] A. Ferretti, C. Prati, and F. Rocca, "Permanent scatterers in sar interferometry," *IEEE Trans. Geosci. Remote Sens.*, vol. 39, no. 1, pp. 8–20, 2001.

[19] Y. Álvarez, Y. Rodriguez-Vaqueiro, B. Gonzalez-Valdes, F. Las-Heras, and A. García-Pino, "Fourier-based imaging for subsampled multistatic arrays," *IEEE Trans. Antennas Propag.*, vol. 64, no. 6, pp. 2557–2562, Jun. 2016.

[20] E. Kpré, C. Decroze, M. Mouhamadou, and T. Fromenteze, "Computational imaging for compressive synthetic aperture interferometric radiometer," *IEEE Trans. Antennas Propag.*, vol. 66, no. 10, pp. 5546–5557, Oct. 2018.

[22] A. R. Thompson, J. M. Moran, and G. W. Swenson, *Interferometry and Synthesis in Radio Astronomy*. John Wiley and Sons, 2001.

[23] J. A. Nanzer, "Millimeter-wave interferometric imaging sensors," in *SENSORS, 2013 IEEE*, Nov 2013, pp. 1–4.

[24] D. Soncco, C. Barbanson, M. Nikolova, A. Almansa, and Y. Ferrec, "Fast and accurate multiplicative decomposition for fringe removal in interferometric images," *IEEE Trans. Comput. Imaging*, vol. 3, no. 2, pp. 187–201, Jun. 2017.

[25] J. A. Nanzer and R. L. Rogers, "Human presence detection using millimeter-wave radiometry," *IEEE Trans. Microw. Theory Techn.*, vol. 55, no. 12, pp. 2727–2733, Dec. 2007.

[26] M. Born, E. Wolf, A. B. Bhatia, P. C. Clemmow, D. Gabor, A. R. Stokes, A. M. Taylor, P. A. Wayman, and W. L. Wilcock, *Principles of Optics: Electromagnetic Theory of Propagation, Interference and Diffraction of Light*, 7th ed. Cambridge University Press, 1999.

[27] C. S. Ruf, C. T. Swift, A. B. Tanner, and D. M. Le Vine, "Interferometric synthetic aperture microwave radiometry for the remote sensing of the earth," *IEEE Trans. Geosci. Remote Sens.*, vol. 26, no. 5, pp. 597–611, Sep. 1988.

[28] K. van 't Klooster, "A few examples of interferometry applications in space-related active and passive remote sensing," in *2004 Second International Workshop Ultrawideband and Ultrashort Impulse Signals (IEEE Cat. No.04EX925)*, 2004, pp. 55–58.

[29] T. Amiot, F. Douchin, E. Thouvenot, J. C. Souyris, and B. Cugny, "The interferometric cartwheel: a multi-purpose formation of passive radar microsatellites," in *IEEE International Geoscience and Remote Sensing Symposium*, vol. 1, 2002, pp. 435–437 vol.1.

[30] P. Bei and W. Ji, "2-d frequency spectrum features and error analysis for interferometric passive microwave imager," in *2007 International Symposium on Microwave, Antenna, Propagation and EMC Technologies for Wireless Communications*, 2007, pp. 1454–1457.

[31] J. A. Nanzer, "Spatial filtering of grating lobes in mobile sparse arrays," in *2016 IEEE Radio and Wireless Symposium (RWS)*, 2016, pp. 26–28.

[32] P. Chatterjee and J. A. Nanzer, "Using platform motion for improved spatial filtering in distributed antenna arrays," in *2018 IEEE Radio and Wireless Symposium (RWS)*, 2018, pp. 253–255.